

# Chapter 5

## Precipitation Strengthening in Face-Centered Cubic Metals

### 5.1 Introduction

The second prevailing strengthening mechanism often used with FCC metals in addition to solid solution strengthening is precipitation strengthening. In this approach, nano- or microscopic particles of a phase distinct from the parent (matrix) material, known as precipitates, are introduced. These precipitates act as obstacles that impede dislocation motion, thereby strengthening the material. Precipitation strengthening can be incredibly effective. For instance, with aluminum alloy 2219, principally alloyed and precipitation strengthened with copper, the yield strength is about 350 MPa, a 70-fold increase relative to pure aluminum [85].

The concept of precipitation strengthening has been around for at least 100 years [52], as have theories elaborating its nature. Much remains poorly understood, however, concerning the fundamentals of precipitation strengthening. Again, this derives from at least two sources of complexity.

The first—similar to the point made in Chapter 1—is due to the difficulty of assessing a material’s plastic response given a distribution of precipitates and dislocations; usually a single dislocation line interacts with many dozens of precipitates simultaneously, and the overall response of the material is due to the accumulation of many dislocation lines interacting in this way. Plasticity of pure metals is already prohibitively complex, and the addition of precipitates only makes things worse. The second source of complexity is the nature of the interaction between an individual precipitate and a dislocation line; we will discuss this interaction in detail throughout the chapter, but we give a brief account here. As a dislocation approaches a precipitate it may experience long-range interactions via a number of mechanisms that can alter its trajectory. Once the line collides with the precipitate, it has two basic options for continuing on past the precipitate (although these aren’t the only ones!): it can either cut the precipitate or loop around it. The cutting process can be highly complex and subject to numerous physical processes—involving, for instance, the formation of a step on the surface of the precipitate—that are difficult to characterize. If looping occurs, afterwards a dislocation loop known as an Orowan loop is left behind, further complicating the long- and short-range interactions. Once again, dislocation dynamics is a tool than can aide in overcoming both of these sources of complexity.

The discussion above makes it clear that the introduction of precipitates into DD requires the consideration of a number of possible effects and interactions. A number of researchers have utilized three-dimensional DD simulations to study precipitation-strengthened materials. However, all of these approaches have a number of shortcomings that make them inappropriate for many materials. First, only spherical [110–114, 116, 117, 119, 120, 122, 137, 139, 153, 164] and cuboidal [74, 140, 171] precipitates have been considered to date, whereas many precipitates have more complex geometries. For instance, precipitates in the Al-Cu system are disk-shaped platelets. Second, only precipitates with purely dilatational lattice misfits—meaning the mismatch between the precipitate and matrix

lattices is purely volumetric—have been used. In many materials the precipitate misfit is strongly non-dilatational, and neglecting this can lead to large errors in the long-range dislocation-precipitate interactions. The numerical approaches of Shin et al. [153], Takahashi and Ghoniem [164], and Crone et al. [34] could be applied to precipitates of any shape and misfit, however they are computationally expensive and prohibitive for the study of bulk material response. We make it a goal to design an algorithm that is computationally inexpensive, so that the interactions between many precipitates and many dislocation lines can be simulated efficiently. And lastly, existing algorithms may miss dislocation-precipitate contact interactions if the time step size is too large, just like we discussed in Chapter 2 with dislocation line collisions. Missing these collisions between dislocations and precipitates can lead to significant inaccuracies, for example failing to capture the formation of an Orowan loop around a precipitate.

Given the shortcomings found in existing DD precipitate formulations, we have developed a new formulation. Our goal was to allow for DD simulations with arbitrarily shaped ellipsoids having arbitrary misfits, and to ensure reliable dislocation-precipitate collision detection. We choose an ellipsoidal precipitate geometry because ellipsoidal inclusions (and inhomogeneities) are well studied in elasticity theory and many common precipitate geometries are well approximated as ellipsoids (e.g., disk, rods, etc.) Another important feature of dislocation-precipitate interactions is cutting: after a dislocation collides with a precipitate, it may cut through the precipitate if the applied stress is high enough. We have incorporated the ability to capture these cutting events in the new formulation. In the first section of this chapter, we will develop all of these features in detail.

With the new algorithm developed and implemented in **ParaDiS**, we will then go on to study plasticity in aluminum-copper alloys, which are of relevance to the automotive and aerospace industries (to name a few) in the form of the 2000 series alloys. For example, aluminum alloy 2219 is alloyed with 5.8-6.8 wt.% Cu (and a few other constituents with 0.4 wt.% or less). We first study

the Orowan looping behavior with periodic arrays of precipitates, showing the effects of precipitate shape and misfit, and then present results for bulk deformation.

## 5.2 Computational Methods

### 5.2.1 Overview

In our formulation, precipitates interact with dislocations in two ways: 1) by exerting long-range forces on dislocations through their misfit fields and 2) through contact and short-range interactions at the precipitate's surface and within the precipitate. Computation of the misfit field is accomplished by treating the precipitate as an Eshelby inclusion of predefined misfit. Incorporation of the contact/short-range interactions is more complex. If a precipitate is semi-coherent or incoherent, transmission of the dislocation into the precipitate will be very difficult. This means the dislocation should be arrested at the surface of the precipitate. If a precipitate is coherent, the dislocation may transmit readily, but the process of cutting through the precipitate may be resisted by a number of complex mechanisms. In our formulation, we reproduce these short-range and contact behaviors with the following approach. Upon initial contact, all nodes are pinned—their velocities are set to zero—at the surface of a precipitate. “Cutting” then occurs by simply un-pinning the node and allowing it to move through the precipitate. Additional resistance may be imposed while the dislocation moves through the precipitate, or the cutting process may be entirely lumped onto the surface of the precipitate in terms of the pinning and un-pinning of nodes.

In order to implement this approach, we will need to develop four key algorithms: 1) collision detection and Orowan loop formation, 2) remeshing at a precipitate's surface, 3) cutting of precipitates and releasing nodes, and 4) force calculation due to a precipitate's misfit. We now step through each of these in detail.

### 5.2.2 Mathematical representation of precipitates

In our approach, precipitates are treated as ellipsoids of arbitrary aspect ratio and arbitrary orientation in space. Over the course of a simulation, each precipitate's geometry is fixed—it does not change shape, orientation, or location. In reality, it is well known that the process of a dislocation cutting a precipitate introduces a step around the circumference of the precipitate, thereby altering its shape. Hence, in materials where precipitates are shearable, the precipitate geometry can change significantly if it is cut repeatedly. Here we neglect this effect for simplicity and computational efficiency; allowing for precipitates with such complex geometries would be prohibitively expensive for large-scale simulations (see Takahashi and Ghoniem [164] for an example of an algorithm than can account for these effects).

To simplify the geometry and mathematics, we use Pope's algorithms for ellipsoids (from which we borrow a number of techniques utilized in this chapter) [135]. In his approach, an ellipsoid is characterized by it's center position,  $\mathbf{c}$ , and the matrix  $A$ , defined as

$$A \equiv U\Sigma^2U^T \quad (5.1)$$

where

$$U = \begin{bmatrix} \mathbf{u}_1 & \mathbf{u}_2 & \mathbf{u}_3 \end{bmatrix}, \quad (5.2)$$

$$\Sigma = \begin{bmatrix} 1/r_1 & 0 & 0 \\ 0 & 1/r_2 & 0 \\ 0 & 0 & 1/r_3 \end{bmatrix}, \quad (5.3)$$

$T$  is the transpose operator,  $\mathbf{u}_i$  is the unit (column) vector pointing along the  $i$ th principal axis, and  $r_i$  is the radius along that axis. The meaning of  $A$  can be clarified by comparing the equation of an

ellipsoid in its principal coordinate system,

$$\frac{(x - x_c)^2}{r_1^2} + \frac{(y - y_c)^2}{r_2^2} + \frac{(z - z_c)^2}{r_3^2} = 1, \quad (5.4)$$

with the equation of the ellipsoid in the coordinate system specified by  $U$ ,

$$(\mathbf{x} - \mathbf{c})^T A (\mathbf{x} - \mathbf{c}) = 1, \quad (5.5)$$

where  $\mathbf{x} = (x, y, z)$  and  $\mathbf{c} = (x_c, y_c, z_c)$  (in a different coordinate system from Eq. (5.4), however).

Note that for a sphere, if we choose the standard basis as axes, then  $A = r_s^{-2} I$  where  $r_s$  is the radius of the sphere and  $I$  is the identity matrix.

As input, the user must specify a *.prec* file, which contains all information for the precipitate microstructure. For each precipitate, we specify its center position  $\mathbf{c}$ , its radii  $r_1$ ,  $r_2$ , and  $r_3$ , its principal axis directions  $\mathbf{u}_1$ ,  $\mathbf{u}_2$ , and  $\mathbf{u}_3$ , its eigenstrain tensor (discussed in Section 5.2.6), and parameters controlling the cutting behavior (discussed in Section 5.2.5).

We will show below that the Cholesky decomposition of  $A$ ,

$$A = LL^T \quad (5.6)$$

is also a useful quantity. For each precipitate, the matrices  $A$ ,  $U$ ,  $L^T$ ,  $L^{-T}$ , and  $L^{-1}L^{-T}$  are needed repeatedly throughout a simulation, so they are tabulated and stored during initialization.

### 5.2.3 Collision detection

In order to ensure that Orowan loops form properly, we need to be able to capture the collision of dislocation segments with precipitates. Other DD codes with precipitate capabilities handle

dislocation-precipitate “collisions” by simply setting the dislocation velocity to zero when inside the precipitate (by either making the drag coefficient or friction stress infinite [114, 138]). However, if the time step is large enough for a colliding dislocation segment to overstep a precipitate completely in one time step, this algorithm will miss the collision. We will opt instead to employ a formal *collision detection* algorithm, where collisions are detected and handled directly rather than relying on a modified mobility law to capture them. In Chapter 2, we showed that the interval halving method can effectively be applied to detect segment-segment collisions. Here, we show that it can also be utilized for the problem of dislocation-precipitate collisions. Recall that all this method requires is the ability to compute the minimum distance between two objects at any point in time. Hence we must develop a method for computing the minimum distance between a line segment and an ellipsoid; this solution is presented in the next section. With this capability, the algorithm is identical to that discussed in Chapter 2. When one node of a segment is already pinned at the surface of the precipitate—as occurs when an Orowan loop is forming—the detection of a collision is much simpler and can be accomplished analytically. We present a collision detection algorithm for this case of “looping” segments in Section 5.2.3.

### **Minimum distance calculation for interval halving method**

To use the interval halving method, all we need is the ability to calculate the minimum separation distance between the two objects of interest at any snapshot in time. Here, we are interested in the collision of a linear dislocation segment with an ellipsoidal inclusion.

In order to compute the minimum separation distance between a line segment with end points  $\mathbf{x}_1$  and  $\mathbf{x}_2$ , and an ellipsoid characterized by  $A$  and  $\mathbf{c}$ , we must solve the following constrained

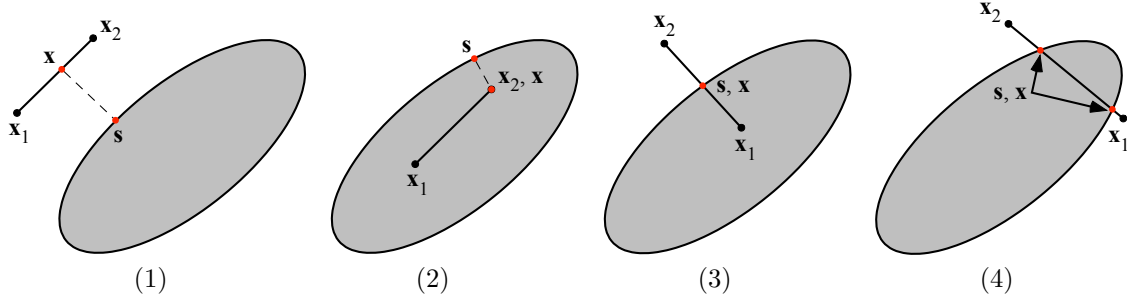


Figure 5.1: Depictions of cases for computing the minimum separation distance between a line segment and an ellipsoid.

minimization problem [135]:

$$\begin{aligned} \underset{\mathbf{x}, \mathbf{s}}{\text{minimize}} \quad & d = \frac{1}{2} \mathbf{y}^T L^{-1} L^{-T} \mathbf{y} + (\mathbf{c} - \mathbf{x})^T L^{-T} \mathbf{y} \\ \text{subject to} \quad & \mathbf{x} = (1 - \alpha)\mathbf{x}_1 + \alpha\mathbf{x}_2, \alpha \in [0, 1] \end{aligned} \quad (5.7)$$

$$\mathbf{y}^T \mathbf{y} = 1$$

where

$$\mathbf{y} \equiv L^T (\mathbf{s} - \mathbf{c}). \quad (5.8)$$

The constraints enforce that points  $\mathbf{x}$  and  $\mathbf{s}$  reside on the line segment and ellipsoid's surface, respectively (see Fig. 5.1). In the case of a sphere, this minimization problem can be solved analytically. A numerical solution is usually required for an arbitrary ellipsoid. Below we present first the solution for a sphere, and then the general ellipsoid solution.

#### *Spherical case*

We consider a sphere of radius  $r_s$  centered on  $\mathbf{c}$ . We must assess the solution for four different configurations, as shown in Fig. 5.1.

##### *Case 1: Segment external to sphere*

First, we consider the case where the segment is external to the sphere. In this case, the distance between the surface of the sphere and any point in the line segment is simply

$$d(\alpha) = \|\mathbf{x}(\alpha) - \mathbf{c}\| - r_s. \quad (5.9)$$

We can find the minimum point by solving

$$\frac{\partial d(\alpha_{\min})}{\partial \alpha} = 0. \quad (5.10)$$

Since both the line segment and sphere are convex, there will be a unique minimum. The solution is

$$\alpha_{\min} = \frac{(\mathbf{x}_1 - \mathbf{x}_2) \cdot (\mathbf{x}_1 - \mathbf{c})}{\|\mathbf{x}_1 - \mathbf{x}_2\|^2}. \quad (5.11)$$

If  $\alpha_{\min} \notin [0, 1]$  is returned, the closest endpoint is the minimizer (i.e.,  $\alpha_{\min} < 0 \rightarrow \alpha_{\min} = 0$  and  $\alpha_{\min} > 1 \rightarrow \alpha_{\min} = 1$ ).

*Case 2: Segment internal to sphere*

If both endpoints are internal to the sphere, i.e.,  $\|\mathbf{x}_1 - \mathbf{c}\| < r_s$  and  $\|\mathbf{x}_2 - \mathbf{c}\| < r_s$ , then whichever end point is furthest from  $\mathbf{c}$  is the minimizer:

$$\alpha_{\min} = \begin{cases} 0 & \|\mathbf{x}_1 - \mathbf{c}\| > \|\mathbf{x}_2 - \mathbf{c}\| \\ 1 & \text{otherwise} \end{cases} \quad (5.12)$$

and  $d(\alpha_{\min}) = r_s - \|\mathbf{x}(\alpha_{\min}) - \mathbf{c}\|$ . Note that if  $\|\mathbf{x}_1 - \mathbf{c}\| = \|\mathbf{x}_2 - \mathbf{c}\|$  the solution is degenerate.

*Case 3: Segment pierces sphere once*

If the segment pierces the sphere once, then the minimizer is the point of intersection between the line segment and the sphere. To find this point, we solve the quadratic expression

$$\|\mathbf{x}(\alpha_{\min}) - \mathbf{c}\| = r_s, \quad (5.13)$$

which has the solution

$$\alpha_{\min} = \frac{-b \pm \sqrt{b^2 - 4ac}}{2a} \quad (5.14)$$

where

$$a = \|\mathbf{x}_1 - \mathbf{x}_2\|^2 \quad (5.15)$$

$$b = -2(\mathbf{x}_1 - \mathbf{x}_2) \cdot (\mathbf{x}_1 - \mathbf{c}) \quad (5.16)$$

$$c = \|\mathbf{x}_1 - \mathbf{c}\|^2 - r_s^2. \quad (5.17)$$

Of course the root with  $\alpha_{\min} \in [0, 1]$  must be selected, and  $d(\alpha_{\min}) = 0$ .

#### *Case 4: Segment pierces sphere twice*

In this case, both endpoints are external to the sphere and the segment pierces the sphere twice; this is a degenerate version of the former case. We can detect this case by first solving for  $\alpha_{\min}$  under the assumption that the segment does not pierce the sphere (Case 1), and if  $d(\alpha_{\min}) < 0$  then the segment pierces twice. We can then simply set  $d = 0$ .

#### *Ellipsoidal case*

##### *Case 1: Segment external to ellipsoid*

The general case for an arbitrary ellipsoid has no analytical solution. Instead, we numerically determine the minimum distance as follows. First, we develop a numerical scheme for finding the point on the surface of the ellipsoid that minimizes the distance to a given point  $\mathbf{p}$ . Then, we apply

this scheme to minimize the separation distance along a line segment.

The position  $\mathbf{s}$  on the surface which minimizes the distance to an arbitrary point  $\mathbf{p}$  solves the following minimization problem:

$$\begin{aligned} \underset{\mathbf{y}}{\text{minimize}} \quad d &= \frac{1}{2}\mathbf{y}^T L^{-1} L^{-T} \mathbf{y} + (\mathbf{c} - \mathbf{p})^T L^{-T} \mathbf{y} \\ \text{subject to} \quad \mathbf{y}^T \mathbf{y} &= 1 \end{aligned} \quad (5.18)$$

where  $\mathbf{y}$  is defined in Eq. (5.8). This is identical to Eq. (5.7) but with the line segment constraint lifted. To solve this problem we employ Newton's method with a Lagrange multiplier. Introducing the function

$$\Lambda(\lambda, \mathbf{y}) = d(\mathbf{y}) + \lambda(1 - \mathbf{y}^T \mathbf{y}) \quad (5.19)$$

where  $\lambda$  is the Lagrange multiplier, we can minimize the distance while enforcing the constraint to stay on the ellipsoid's surface by finding the solution to  $\partial\Lambda/\partial\mathbf{y} = \mathbf{0}$ ,  $\partial\Lambda/\partial\lambda = 0$ . We can express these conditions with the nonlinear system

$$\mathbf{0} = \begin{bmatrix} L^{-1}L^{-T} & -2\mathbf{y} \\ -\mathbf{y}^T & 0 \end{bmatrix} \begin{bmatrix} \mathbf{y} \\ \lambda \end{bmatrix} + \begin{bmatrix} L^{-1}(\mathbf{c} - \mathbf{p}) \\ 1 \end{bmatrix} \quad (5.20)$$

whose Jacobian is

$$J = \begin{bmatrix} (L^{-1}L^{-T} - 2\lambda I) & -2\mathbf{y} \\ -2\mathbf{y}^T & 0 \end{bmatrix}. \quad (5.21)$$

We apply Newton's method to solve this system. For an initial guess, we use the intersection point between the ray connecting  $\mathbf{p}$  and  $\mathbf{c}$  and the ellipsoid's surface, given by [135]

$$\mathbf{y}_{\text{guess}} = \frac{L^T(\mathbf{p} - \mathbf{c})}{\|L^T(\mathbf{p} - \mathbf{c})\|}. \quad (5.22)$$

Since  $d$  also has a maximum, this approach is not guaranteed to find the minimizer. To protect against finding the maximizer, we check that  $d(\mathbf{y}_{\text{sol}}) \leq d(\mathbf{y}_{\text{guess}})$ , where  $\mathbf{y}_{\text{sol}}$  is the solution obtained by Newton's method. If the method fails to find the minimizer, we set  $\mathbf{y}_{\text{sol}} = \mathbf{y}_{\text{guess}}$ .

With the ability to find the minimum distance to any given point, we then minimize along a line segment by using a numerical minimization scheme. Since both the line segment and precipitate are convex, we are guaranteed to have a unique minimum [48], making  $d(\alpha)$  a unimodal function. The golden section search method [136] is an efficient scheme for derivative-free minimization of unimodal functions, and has been applied in **ParaDiS** for minimum distance calculation.

#### *Case 2: Segment internal to ellipsoid*

As in the spherical case, the minimizer will be one of the endpoints of the segment. Since the approach discussed above for finding the minimum distance between a point and the ellipsoid does not require that  $\mathbf{p}$  lie outside the ellipsoid, we can use the exact same scheme for this case, and the minimum distance is simply  $d(\alpha_{\min}) = \min \{d(0), d(1)\}$ .

#### *Case 3: Segment pierces ellipsoid once*

The solution for this case can be computed analytically; for this reason, we use this solution throughout the code for placing nodes on the surface of precipitates. As in the spherical case, the minimizer is the point of intersection between the line segment and ellipsoid, and we can determine that point by solving the following expression for  $\alpha_{\min}$ :

$$(\mathbf{x}(\alpha_{\min}) - \mathbf{c})^T A (\mathbf{x}(\alpha_{\min}) - \mathbf{c}) = 1 \quad (5.23)$$

where  $\mathbf{x}(\alpha) = (1 - \alpha)\mathbf{x}_1 + \alpha\mathbf{x}_2$ . Again, this yields a quadratic expression with the same solution as Eq. (5.14), but with

$$a = \mathbf{x}_1^T A \mathbf{x}_1 - 2\mathbf{x}_1^T A \mathbf{x}_2 + \mathbf{x}_2^T A \mathbf{x}_2 \quad (5.24)$$

$$b = -2(\mathbf{x}_1 - \mathbf{c})^T A (\mathbf{x}_1 - \mathbf{x}_2) \quad (5.25)$$

$$c = \mathbf{x}_1^T A \mathbf{x}_1 - 2\mathbf{c}^T A \mathbf{x}_1 + \mathbf{c}^T A \mathbf{c} - 1. \quad (5.26)$$

#### *Case 4: Segment pierces ellipsoid twice*

Applying the method for Case 1, we will obtain one of the points of intersection between the line segment and ellipsoid, which will give  $d(\alpha_{\min}) = 0$ ; no additional solution is necessary for this case.

#### **Use of oriented bounding box**

As discussed above for Case 1 with an ellipsoid, minimum distance computation for an arbitrary ellipsoid with an external line segment is computationally expensive. Each distance calculation requires repeatedly rootfinding a  $4 \times 4$  nonlinear system. A collision algorithm that uses this distance computation approach in DD exhibits poor performance; when several hundred or more precipitates are used, distance computation dominates the computational cost. This fact necessitates a more efficient approach.

To make our detection algorithm more efficient, we apply an approach commonly used by the collision detection community: we first test for a collision using a simpler, approximate representation of the precipitate. The oriented bounding box (OBB) is one such representation. In collision detection, the OBB refers to the smallest possible box (rectangular parallelepiped) enclosing an object [48]. For an ellipsoid, the OBB is the box whose faces are normal to  $\mathbf{u}_1$ ,  $\mathbf{u}_2$ , and  $\mathbf{u}_3$  and whose dimensions are  $2r_1$ ,  $2r_2$ , and  $2r_3$ . The minimum distance between a line segment and an OBB can be computed analytically in an efficient manner [146] (although the approach presented in [146]

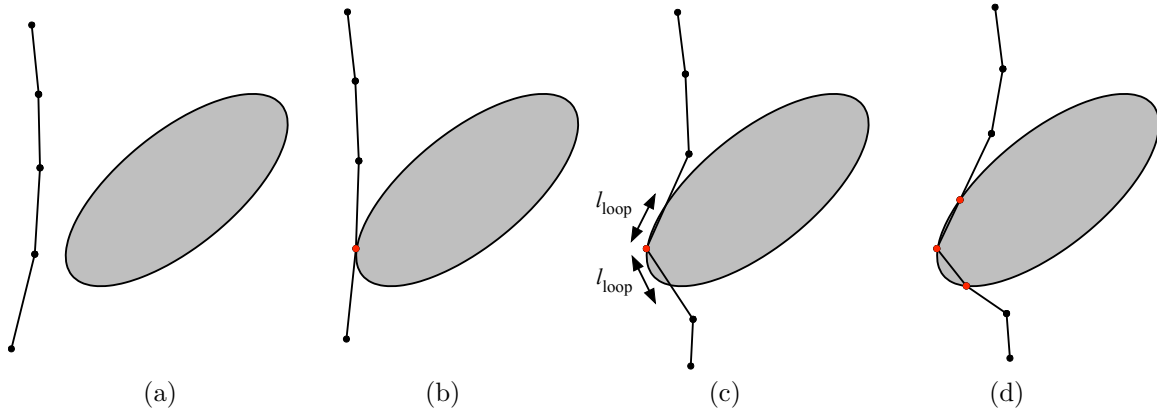


Figure 5.2: Schematic showing the process of Orowan loop formation. Red nodes have collided and are pinned at the precipitate's surface. (a) Dislocation moves towards a precipitate. (b) Initial collision occurs, causing a node to be pinned. (c) Segments rotate about the pinned node. Collisions are ignored within a distance  $l_{\text{loop}}$  of the pinned node. (d) New nodes are added as the segments collide.

is not quite complete<sup>1</sup>). Since an ellipsoid's OBB bounds it in space, any segment that collides with the ellipsoid must necessarily also collide with the ellipsoid's OBB. Hence, we can cheaply screen out segments which are far from colliding by first testing for a collision against the OBB using the interval halving method. Incorporating this step into our detection algorithm improves the efficiency significantly.

### Collisions during Orowan loop formation

In order for Orowan loops to form, we must be able to simulate the process of a dislocation line wrapping around a precipitate. We can consider this process occurring as follows; see Fig. 5.2 for reference. First, a segment makes initial contact and a node becomes pinned at the surface of the precipitate; call this the hinge node. The segments attached to this hinge node will then rotate about it and begin wrapping around the precipitate. Once these segments become tangent to the ellipsoid at the contact point, a point on the segment infinitesimally close will also make contact.

---

<sup>1</sup>The case where the minimizing point on the box is in the middle of an edge is not treated correctly. To solve this case, the minimum distance between the edge and dislocation line segment must be computed using the minimum distance expression for two line segments, which is known analytically [17, 48, 146].

Thus, only implementing the above algorithm would result in Orowan loops comprised of infinitely many dislocation segments. To overcome this issue, if a segment has one node which is already in contact with a precipitate, we do not search for collisions over a length  $l_{\text{loop}}$  from that node; we refer to this as the *looping length*. In order to ensure that the looping process is accurately captured, we set this looping length equal to half the smallest radius of curvature of the precipitate, i.e.,

$$l_{\text{loop}} = \frac{1}{2} \left( \frac{r_{\min}^2}{r_{\max}} \right) \quad (5.27)$$

where  $r_{\min} = \min\{r_1, r_2, r_3\}$  and  $r_{\max} = \max\{r_1, r_2, r_3\}$ . With high aspect ratio ellipsoids, this looping length can be quite small and result in very small dislocation segments; this motivates the remeshing algorithm presented in Section 5.2.4.

Detection of a looping collision is much simpler than a general collision; we demonstrate the looping collision algorithm in Fig. 5.3. We enforce the loop length condition by ignoring the sections of the segment within  $l_{\text{loop}}$  of the hinge node in the current and old configurations (current and previous time steps), and then assume the trajectory of the truncated segment is linear in space (same as we did with segment-segment collisions). Let the points on the segment a distance  $l_{\text{loop}}$  from the hinge node be  $\mathbf{x}_l(t')$  and  $\mathbf{x}_l(t'+\Delta t)$ , so that the position of this point at any time within the time step is  $\mathbf{x}_l(t'+\beta\Delta t) = (1-\beta)\mathbf{x}_l(t') + \beta\mathbf{x}_l(t'+\Delta t)$  where  $\beta \in [0, 1]$ . Owing to the convex nature of both objects and the constrained motion of a hinged segment, the collision between the precipitate and the truncated segment will always occur along  $\mathbf{x}_l(t'+\beta\Delta t)$ . Hence, collision detection simplifies to determining where the line  $\mathbf{x}_l(t' + \beta\Delta t)$  intersects the precipitate's surface. Mathematically this is stated as: find  $\beta$  such that  $(\mathbf{x}_l(t' + \beta\Delta t) - \mathbf{c})^T A(\mathbf{x}_l(t' + \beta\Delta t) - \mathbf{c}) = 1$ . We have already solved this expression in Case 3 of the ellipsoid minimum distance calculation. If  $\beta \notin [0, 1]$  is returned or a real solution cannot be found (i.e., the discriminant is negative), there is no collision.

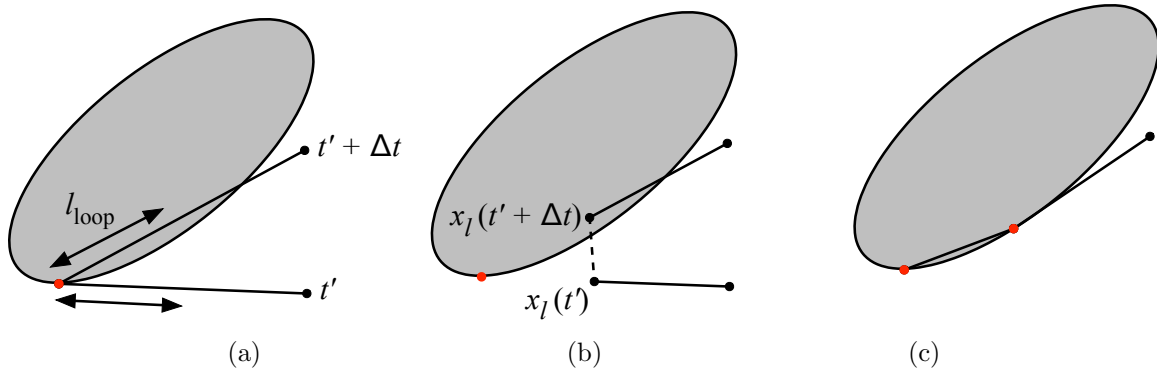


Figure 5.3: Collision algorithm used for looping collisions with hinge segments. (a) Hinge segment positions at time  $t'$  and time  $t' + \Delta t$ . (b) Truncation of segments according to  $l_{loop}$  and determination of the collision point. (c) Final configuration after the collision has been handled.

#### 5.2.4 Remeshing

Having the ability to control the discretization of the dislocation lines pinned on precipitates is important for a number of reasons. Firstly, the above described looping algorithm does not guarantee a uniform and/or consistent discretization around a precipitate, making it desirable to develop a separate algorithm that allows the discretization to be controlled. Secondly, Orowan loops produce stress fields that can interact with other dislocations, and the fidelity of these stress fields will be affected by the quality of the discretization. And thirdly, the cutting algorithm presented below uses the force per unit length exerted on the dislocation line to determine whether a cutting event should occur. The accuracy of this force calculation is sensitive to the discretization; regions of the precipitate surface that are tightly curved require a finer discretization, for instance. The “bulk” remeshing algorithm is not appropriate for dislocation segments pinned at precipitates; it uses the directions of motion of the dislocation segments to determine when remeshing should occur, whereas segments attached to precipitates are immobile. Finally, precipitates are often much smaller than the minimum segment size specified for the bulk,  $l_{min}$ , which would lead to low quality discretizations on precipitates.

For these reasons, we have developed a separate remesh algorithm for segments pinned at precipitates. Overall, the algorithm and code proceed in the same manner as the bulk remesh code, but with slightly different rules for determining when nodes should be removed or segments should be bisected. The algorithm operates based on two input parameters: a minimum angle between dislocation segments,  $\theta_{\min}^P$ , and a minimum segment length,  $l_{\min}^P$ , where the superscript ‘p’ indicates that these parameters apply to segments pinned at precipitates. In contrast, the minimum and maximum segment lengths  $l_{\min}$  and  $l_{\max}$  are specified for the bulk refinement algorithm. Remeshing then proceeds as follows:

A node located at  $\mathbf{r}_0$  pinned at a precipitate is removed if three conditions are met:

1. It is connected to exactly two nodes located at  $\mathbf{r}_1$  and  $\mathbf{r}_2$ , both of which are also pinned at the same precipitate.
2. The distance between the neighbor nodes is less than or equal to the maximum segment length (i.e.,  $\|\mathbf{r}_1 - \mathbf{r}_2\| \leq l_{\max}$ ).
3. The angle between the node’s segments is greater than  $\theta_{\min}^P$  and the angles between all of the neighboring nodes’ segments after the node is removed will also be greater than  $\theta_{\min}^P$ , *OR* one of the node’s segments is shorter than  $l_{\min}^P$  (i.e.,  $\|\mathbf{r}_0 - \mathbf{r}_1\| < l_{\min}^P$  or  $\|\mathbf{r}_0 - \mathbf{r}_2\| < l_{\min}^P$ ).

A segment with nodes located at  $\mathbf{r}_1$  and  $\mathbf{r}_2$  which are both pinned at the same precipitate is bisected using point  $\mathbf{r}_3$  for a new node if two conditions are met:

1. After bisection, the resulting segment lengths are greater than the minimum segment length for precipitates (i.e.,  $\|\mathbf{r}_1 - \mathbf{r}_3\| \geq l_{\min}^P$  and  $\|\mathbf{r}_2 - \mathbf{r}_3\| \geq l_{\min}^P$ ).
2. The segment length is greater than the maximum segment length (i.e.,  $\|\mathbf{r}_1 - \mathbf{r}_2\| > l_{\max}$ ), *OR* the angle formed between one of the nodes and any of its neighbors is less than  $\theta_{\min}^P$ .

The point  $\mathbf{r}_3$  is found by projecting the midpoint of the segment onto the surface of the ellipsoid, while staying within its glide plane, using the solution for Case 3 of the minimum distance calculation.

Generally we specify  $l_{\min}^P \leq l_{\min}$ , however  $l_{\min}^P$  should not be smaller than the segment collision radius (otherwise the segment collision algorithm will collide segments at the precipitate surface). The minimum angle  $\theta_{\min}^P$  provides the main driving force for discretization refinement, and the minimum length  $l_{\min}^P$  imposes a limit on it. With this scheme, ellipsoids with a high aspect ratio will have smaller segments in regions with a small radius of curvature. It generates a fairly uniform discretization with spherical precipitates.

### 5.2.5 Obstacle cutting

With the obstacle cutting algorithm, we address short-range interactions that occur while a dislocation cuts through a precipitate; long-range interactions are addressed in the next section. When a dislocation line intersects a precipitate, many different physical effects can contribute to their interaction. These may include: dislocation transmission across a semi-coherent interface, the formation of a step on the precipitate (chemical strengthening), stacking fault energy or modulus differences between the matrix and precipitate, and the disruption of superlattice ordering [7, 8]. These interactions can be understood in terms of a so-called force-distance curve [86], which characterizes the force resisting transmission of the dislocation as it moves through the precipitate. In this way, we could account for these short-range effects by adding additional forces to the dislocation lines. However, we are interested in studying the interaction of many of dislocation lines with large numbers of precipitates. For these sorts of simulations, the specific details of the contact interactions between dislocations and precipitates will only have a minor effect on the results. Rather, the most important feature to capture is whether or not a dislocation line is impeded by a precipitate.

Using this line of reasoning, we have developed a simple model for obstacle cutting. In this model, aside from the long-range misfit force discussed below, dislocations and precipitates only interact in one way: dislocation nodes may become pinned at the surface of precipitates. Upon contact, all dislocation nodes are treated as pinned at a precipitate's surface. This means they are fixed in place and cannot move. They may be released and rendered mobile again if one of two conditions is reached: 1) the dislocation's velocity upon being released is in the direction of the precipitate's local outward normal  $\mathbf{n}$  (i.e.,  $\mathbf{v} \cdot \mathbf{n} > 0$ ) or 2) a *cutting event* occurs. Determining when cutting events occur requires input from a model of the dislocation-precipitate interaction, for example using atomistic simulations of a dislocation interacting with a periodic array of precipitates. We can think of two different types of models for cutting events: athermal and thermally-activated. Athermal cutting events occur when a minimum stress or force per unit length is applied to the dislocation line in contact with the precipitate. Thermally-activated cutting events occur stochastically on the basis of the energy barrier associated with a cutting event; the energy barrier may be reduced by the application of stress to the dislocation, leading to an increase in the cutting rate. Generally dislocation-precipitate interactions are thought to be athermal [7], except in the case of very small or weak precipitates [8] (for example GP-I zones in Al-Cu [159]).

Note that this approach could also be combined with the friction stress model used by many other researchers to account for the cutting resistance of precipitates [114, 138]. For instance, the initial barrier for transmission into the dislocation could be handled with the cutting model, and a friction stress could be used to account for the actual cutting resistance. The specifics of the cutting model should be selected on the basis of comparisons with experiments and/or other models (such as atomistic simulations).

### 5.2.6 Misfit force calculation

Precipitates are known to interact at a distance with dislocations via two mechanisms: misfit and elastic mismatch. If a precipitate is coherent or semicoherent, and has a lattice constant different from the parent (matrix) material, the resulting misfit generates a stress field in the matrix which can exert forces on dislocation lines. The character of this misfit field is set by the type of misfit (e.g., dilatational and/or shear) and the shape of the precipitate. When a precipitate has elastic constants that differ from the matrix, dislocations can experience additional interaction forces. This elastic mismatch effect is difficult to address for arbitrary geometries and usually requires the use of a numerical solver (like the finite element method [153] or a boundary element method [164]), making it computationally complex and expensive. Furthermore, long-range modulus mismatch effects are often (though not always) second-order relative to misfit effects [8]. For example, Shin et al. [153] found that the Orowan bypassing stress around a spherical precipitate was only altered by 6% when the precipitate and matrix moduli differ by a factor of six. For these reasons, we will neglect long-range modulus mismatch effects and focus only on the misfit force. Note that short-range modulus mismatch effects may still be effectively accounted for through the obstacle cutting model.

The stress field of a misfitting ellipsoidal inclusion in an infinite body is known analytically [123], however the resulting expressions are complicated and difficult to evaluate. Instead, we will develop a numerical approach based on adaptive quadrature over a sphere. We will design the method so that arbitrarily shaped ellipsoids with arbitrary misfit can be considered.

We begin by introducing the idea of an eigenstrain field. In the eigenstrain approach [123], any inelastic strain field, which may vary with position, can be treated as a so-called eigenstrain field, in terms of which the resulting elastic stresses may be calculated. In the context of misfitting inclusions, the eigenstrain is exactly the same as the “transformation strain” imposed on the inclusion,  $\epsilon_{ij}^*$ , after it is has been cut out of the matrix. Here, we will assume that the transformation strain is a constant

throughout the inclusion (no variation with position). Hence, the resulting eigenstrain field of the infinite medium containing an inclusion is equal to  $\epsilon_{ij}^*$  inside the inclusion, and zero everywhere else. The eigenstrain characterizing the misfit for a particular precipitate can be determined using a number of approaches; we will make use of results from density functional theory calculations in our simulations [170]. In Appendix C we present an approach for using atomistics to determine the eigenstrain of a precipitate.

The procedure for determining the stress field is straightforward (below we will use Einstein notation in our derivation). The displacement field external to an inclusion is related to the Green's function by [178]

$$u_i(\mathbf{x}) = \int_{S_0} \sigma_{jk}^* n_k(\mathbf{x}') G_{ij}(\mathbf{x}, \mathbf{x}') dS(\mathbf{x}') \quad (5.28)$$

where  $S_0$  is the surface area of the inclusion,  $n_k(\mathbf{x}')$  is the outward normal unit vector,  $G_{ij}(\mathbf{x}, \mathbf{x}')$  is the elastic Green's function, and  $\sigma_{ij}^*$  is the eigenstress tensor, related to the eigenstrain by Hooke's law,  $\sigma_{ij}^* = C_{ijkl}\epsilon_{kl}^*$ . For the case of an isotropically elastic solid, the elastic Green's function is [123]

$$G_{ij}(\mathbf{x}, \mathbf{x}') = \frac{1}{8\pi\mu} \left( \delta_{ij} R_{,nn} - \frac{1}{2(1-\nu)} R_{,ij} \right) \quad (5.29)$$

and

$$C_{ijkl} = \frac{2\mu\nu}{1-2\nu} \delta_{ij} \delta_{kl} + \mu (\delta_{ik} \delta_{jl} + \delta_{il} \delta_{jk}) \quad (5.30)$$

where  $\mu$  is the shear modulus,  $\nu$  is Poisson's ratio, and  $R = \sqrt{x^2 + y^2 + z^2}$ . Applying the definition of strain  $\epsilon_{ij} = \frac{1}{2}(u_{i,j} + u_{j,i})$  and Hooke's law, we arrive at a stress field outside of the inclusion of

$$\sigma_{ij}(\mathbf{x}) = \frac{1}{2} C_{ijkl} \int_{S_0} \sigma_{nm}^* n_m(\mathbf{x}') [G_{kn,l}(\mathbf{x}, \mathbf{x}') + G_{ln,k}(\mathbf{x}, \mathbf{x}')] dS(\mathbf{x}') \quad (5.31)$$

Hence, the stress field can be determined by computing a surface integral over the ellipsoidal surface  $S_0$ .

We proceed with calculation of the force on a node due to the misfit field of a precipitate as follows. We take the  $\mathbf{x}'$  coordinate system as the principal coordinate system of the ellipsoid, and define the coordinate transformation

$$x'_1 = r_1 \sin \theta \cos \phi \quad (5.32)$$

$$x'_2 = r_2 \sin \theta \sin \phi \quad (5.33)$$

$$x'_3 = r_3 \cos \theta, \quad (5.34)$$

where  $\theta \in [0, 2\pi)$  and  $\phi \in [0, \pi)$  are the usual spherical coordinates. Using this transformation, the ellipsoid's surface is defined as

$$S_0 = \{\mathbf{x}'(\theta, \phi) \mid \theta \in [0, 2\pi), \phi \in [0, \pi)\} \quad (5.35)$$

and  $dS(\mathbf{x}') = \|(\partial \mathbf{x}' / \partial \theta) \times (\partial \mathbf{x}' / \partial \phi)\| d\theta d\phi$ . Noting that the outward unit normal of the precipitate is

$$n_i(\mathbf{x}') = \frac{x'_i / r_i^2}{\sqrt{x'_1^2 / r_1^4 + x'_2^2 / r_2^4 + x'_3^2 / r_3^4}}, \quad (5.36)$$

the integral Eq. (5.31) can be expressed as

$$\sigma_{ij}(\mathbf{x}) = \frac{1}{2} C_{ijkl} \int_0^\pi \int_0^{2\pi} \sigma_{nm}^* n_m(\mathbf{x}') [G_{kn,l}(\mathbf{x}, \mathbf{x}') + G_{ln,k}(\mathbf{x}, \mathbf{x}')] \|(\partial \mathbf{x}' / \partial \theta) \times (\partial \mathbf{x}' / \partial \phi)\| d\theta d\phi. \quad (5.37)$$

This integral can be evaluated to give the stress field at any field point  $\mathbf{x}$  using the adaptive quadrature function `quad2d` in MATLAB. For an example of a misfitting ellipsoid's stress field, see the plots given in Fig. 5.6.

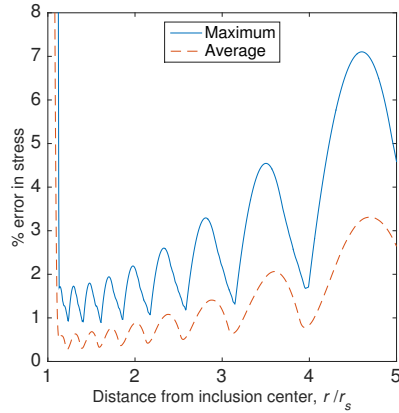


Figure 5.4: Percent error in the numerical stress field of a spherical inclusion with dilatational misfit as a function of distance from the center of the sphere. The numerical stress field was computed with a transformation parameter of  $\alpha = r_s$  where  $r_s$  is the radius of the sphere. Shown are the errors obtained considering all possible rays passing through the inclusion's center, in terms of both the average error of the three non-zero stress components (one radial and two hoop stress components) and the maximum error of the three components, at each distance.

Using this approach, we precompute the misfit stress field of the inclusion on a computational grid. Since the stress field around an inclusion in three-dimensions decays as  $1/R^3$ , the field varies much more rapidly near the inclusion, requiring a finer grid there. To address this, we transform a uniform grid on the biunit cube, termed the transformed domain with  $x_i^t \in [-1, 1]$ , using the transformation function  $x_i = \alpha \tan^{-1} x_i^t$ , where  $\alpha$  is a parameter that controls the grid spacing. Since the grid is uniform in the transformed domain, stress values between grid points can be obtained using simple linear interpolation in the transformed domain. To demonstrate the accuracy of this approach, we show a comparison between the analytical stress field for a dilatational sphere external to the sphere and the numerical field in Fig. 5.4 using a  $50 \times 50 \times 50$  grid with  $\alpha = r_s$ , the radius of the sphere. Except very near the surface where the stress field is discontinuous, within  $5r_s$  of the sphere the error is on average less than about 3% and is less than about 7%.

The last step is to determine the force on the node of a linear dislocation segment. This is found by integrating the Peach-Koehler force over the length of the segment, weighted by the linear shape

function of the segment. For a segment with Burgers vector  $\mathbf{b}$  and line direction  $\boldsymbol{\xi}$  connecting nodes 1 and 2, the force on node 1 is

$$\mathbf{f}_1 = \left[ \int_0^1 s \sigma_{ij} ((1-s)\mathbf{x}_1 + s\mathbf{x}_2) ds \cdot \mathbf{b} \right] \times \boldsymbol{\xi}. \quad (5.38)$$

To evaluate this line integral we use Gauss quadrature.

Since computation of the pretabulated stress field can be time consuming ( $\sim 12$  hours on a single CPU with a  $50 \times 50 \times 50$  grid, though it parallelizes readily using a `parfor` loop since each grid point is independent) and storage of the stress field can be memory intensive, we compute the field non-dimensionally and then scale it for a specific precipitate as appropriate. In this way, a single stress field file can be used for many different precipitates with the same aspect ratio and (relative) misfit. For example the simulations below with  $\theta'$  precipitates in Al-Cu all used the same misfit field file.

### 5.3 Simulations of Precipitate-Dislocation Interactions

We now apply the new precipitates code to study plasticity in the aluminum-copper system. Four different precipitates are observed during aging in this system [124]. In this work we will only focus on one: the metastable  $\theta'$  precipitate. We select this precipitate for several reasons. For peak- and over-aged materials,  $\theta'$  precipitates are thought to be strong contributors to precipitation strengthening [151,155], so understanding their interactions with dislocations is key to understanding strengthening in these alloys. They have a tetragonal lattice with a composition of  $\text{Al}_2\text{Cu}$ , and are semicoherent with the aluminum matrix. Their semicoherent misfit makes the transmission of dislocations into the precipitate lattice difficult, so that Orowan looping is the predominant mode for bypassing  $\theta'$  precipitates [142,148]. This means we can treat them as impenetrable in our model,

and do not have to worry about the details of the cutting process. Finally,  $\theta'$  precipitates are high aspect ratio platelets (as are all precipitates in the aluminum-copper system) and have a highly non-dilatational misfit [170]; this makes them useful for testing the newly developed capabilities.

We will first study the process of Orowan loop formation by simulating the interaction between a dislocation line and a periodic array of precipitates. In particular, we will determine how the shear stress necessary for Orowan looping,  $\tau_{\text{loop}}$ , varies with precipitate orientation, precipitate spacing, and dislocation character. We will then go on to present a few results showing the behavior of an overaged aluminum-copper alloy with a realistic precipitate microstructure.

### 5.3.1 Orowan looping

Orowan looping around spherical inclusions has been heavily studied. The simplest analysis was carried out by Orowan [132], where using a constant line tension model he showed that the applied shear stress necessary to form an Orowan loop is

$$\tau_{\text{loop}} = \frac{2T}{b(L - d)} \quad (5.39)$$

where  $T$  is the line tension,  $b$  is the magnitude of the Burgers vector,  $L$  is the separation distance between precipitate centers, and  $d$  is the precipitate diameter. Often the line tension is approximated as  $T \approx \mu b^2/2$  [75], giving

$$\tau_{\text{loop}} = \frac{\mu b}{(L - d)}. \quad (5.40)$$

However, this result is overly simplistic in a number of ways, all of which were elucidated very nicely by Bacon et al. [10]. It is well known that the dislocation line tension is not a constant, but instead varies with character angle [75] so that the looping stress will depend on the orientation of the dislocation line. Furthermore, because of the fact that adjacent bowing sections of dislocation

line screen each other elastically, the line tension depends on the precipitate spacing. This effect can be taken into account through the outer cut-off radius  $R_c$  used when computing the dislocation line's elastic energy. There are two limits to the elastic screening effect. When  $d \gg L - d$ , the bowing section behaves as an isolated dislocation line so that  $R_c = L - d$ . And when  $d \ll L - d$ , the dislocation lines on opposing sides of the precipitate interact most strongly, making  $R_c = d$ . Bacon et al. showed that taking  $R_c = X$ , where

$$X \equiv [(L - d)^{-1} + d^{-1}]^{-1}, \quad (5.41)$$

the harmonic mean of  $L - d$  and  $d$ , captures the looping behavior over the full range of  $d/(L - d)$  values. Combining all of these effects gives the Bacon-Kocks-Scattergood (BKS) relationship [10]:

$$\tau_{\text{BKS}} = A \frac{\mu b}{(L - d)} \left[ \ln \left( \frac{X}{r_c} \right) + B \right], \quad (5.42)$$

where  $r_c$  is the core radius,  $B$  is a fitting constant, and  $A = 1/[2\pi(1 - \nu)]$  or  $1/(2\pi)$  for a dislocation line that is initially screw or edge, respectively [10].

Other researchers have investigated additional effects on the Orowan looping process. Duesbery and Sadananda [45] studied the influence of a dilatational misfit on the looping behavior around spherical inclusions (although they allowed the dislocation to penetrate the precipitates in their simulations), showing that the interaction between the elastic field of the precipitate and the dislocation was strongly dependent upon the height of the glide plane relative to the sphere's centerline and the initial character angle. Shin et al. [153] and Takahashi and Ghoniem [164] considered the effect of a modulus mismatch, showing a relatively modest influence on the looping stress. Monnet et al. [120] studied Orowan looping in body-centered cubic (BCC) metals with a temperature-dependent mobility law. The looping stress for random distributions of impenetrable precipitates has also been

studied by Mohles and coworkers [112, 113], in addition to others.

Orowan looping around non-spherical precipitates is less well studied. With this work, we will examine the influence of a high aspect ratio ellipsoidal geometry on dispersion strengthening, and the strengthening provided by the lattice mismatch of a  $\theta'$  precipitate. We will show that misfit strengthening can be significant when precipitates are closely spaced and that dispersion strengthening with ellipsoids is not well characterized by the BKS expression, but instead necessitates the development of a new model based on the formation of a dislocation dipole.

### Simulation setup

We will consider the Orowan looping of both edge and screw dislocations. We use the (111) glide plane that intersects the centroid of the precipitate, and a Burgers vector of  $\frac{b}{\sqrt{2}}[01\bar{1}]$ . All precipitates in the Al-Cu system have {001} habit planes. As shown in Fig. 5.5(a), there are two possible precipitate geometries. The “Type A” geometry corresponds to the Burgers vector being parallel to plane of the precipitate, and the “Type B” geometry corresponds to the Burgers vector being at  $60^\circ$  to the precipitate in the glide plane. It is important to point out that because the precipitate intersects the glide plane obliquely in both geometries, the misfit field of the precipitate in the glide plane may be asymmetrical. This means that in general, a dislocation will behave differently when approaching a precipitate from opposing sides. Hence, to fully assess the looping behavior, we need to consider looping starting on both sides of the precipitate. Note that in the absence of a misfit field, looping from either side is equivalent. Fig. 5.5(b) shows the two types of precipitates in the glide plane as viewed by an edge (left) and a screw (right) dislocation. Considering both edge and screw dislocations and loading from both sides with both geometry types, we have 8 difference cases to compute. We will additionally compute looping stresses without a misfit field to assess its role in strengthening.

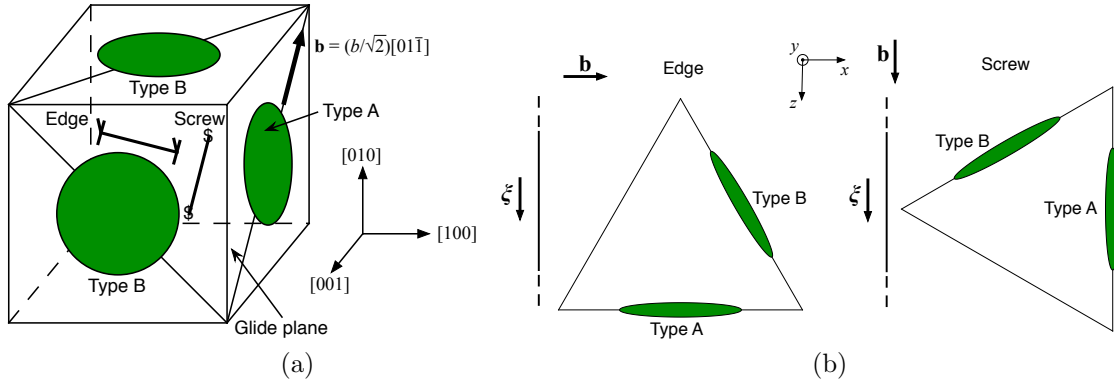


Figure 5.5:  $\theta'$  precipitate geometry for Orowan looping simulations. (a) Unit cell view. The Burgers vector is  $\mathbf{b} = \frac{b}{\sqrt{2}}[01\bar{1}]$  and the glide plane normal is  $\mathbf{n} = (111)$ . Type A precipitates reside in (100) planes, so that the Burgers vector is parallel to the habit plane. Type B precipitates are in (010) or (001) planes, forming a  $60^\circ$  angle with the Burgers vector in the glide plane. Edge and screw dislocation line directions are shown. (b) Glide plane view for edge (left) and screw (right).  $\xi$  is the line direction vector. Only showing the [010] Type B precipitate, which was used in simulations.

To compute the Orowan looping stress, we perform simulations under a constant stress and monitor for looping. As shown in Fig. 5.5(b), we rotate the geometry so that the glide plane normal in the coordinate system of the simulation cell is (010) (in the  $y$ -direction) and the line direction is [001] (in the  $z$ -direction), and we apply a shear stress of  $\tau_{xy}$  or  $\tau_{yz}$ . Periodic boundary conditions are used to simulate an infinite array of precipitates. The stress is increased in 2.5 MPa increments until looping occurs. We repeat this process with a variety of precipitate separation distances,  $L$ , to populate  $\tau_{\text{loop}}$  versus  $L/d$  curves. The maximum segment length was set to  $L/l_{\max} = 10$  for all cases except Type A with a screw dislocation, which required  $L/l_{\max} = 40$  to attain a convergent solution. The time integration tolerance was set to  $r_{\text{tol}} = 0.1b$ . To resolve the shape of the Orowan loops at the outer edges of the ellipsoid, the precipitate remesh parameters were set to  $\theta_{\min}^P = 170^\circ$  and  $l_{\min}^P = 5b$ . Values used for other parameters are given in Table 5.1; in the section discussing precipitate microstructures we will justify our choice for the precipitate radii.

Table 5.1: Parameter values used for simulations of Al-Cu.

Property	Parameter	Value
Shear modulus	$\mu$	26 GPa
Poisson's ratio	$\nu$	0.35
Burgers vector magnitude	$b$	2.86 Å
Core energy parameter	$E_c$	8.48 GPa [177]
Edge drag coefficient	$B_e$	111 $\mu$ Pa·s [130]
Screw drag coefficient	$B_s$	180 $\mu$ Pa·s [130]
Core radius	$a$	$4b$
Precipitate major radii	$r_1, r_2$	2000 Å
Precipitate aspect ratio	$r_1/r_3$	30

## Results

### Misfit field

We begin by examining the misfit field of the precipitates. In the coordinate system of the precipitate, we use an eigenstrain tensor of

$$\epsilon^* = \begin{bmatrix} 0.007 & 0 & 0 \\ 0 & 0.007 & 0 \\ 0 & 0 & -0.051 \end{bmatrix} \quad (5.43)$$

as obtained by Vaithyanathan et al. [170] for  $\theta'$  precipitates using first principles. Fig. 5.6 shows the shear stress fields  $\tau_{xy}$  and  $\tau_{yz}$  in the glide plane of a periodic array of precipitates for the four geometries considered here. Note that with our sign conventions, positive stresses exert positive forces on the dislocation line (towards the right side of the figure). In both Type A cases, the stress field around each precipitate is antisymmetric across horizontal and vertical axes. Because of this symmetry, the looping process is equivalent when approached from either side by a dislocation line. This is similar to the misfit field exerted on a screw dislocation by a spherical precipitate with dilatational misfit [45]. In contrast, the Type B fields exhibit two-fold symmetry. For these cases, we expect an asymmetric response between the two sides. The Type B edge case is particularly

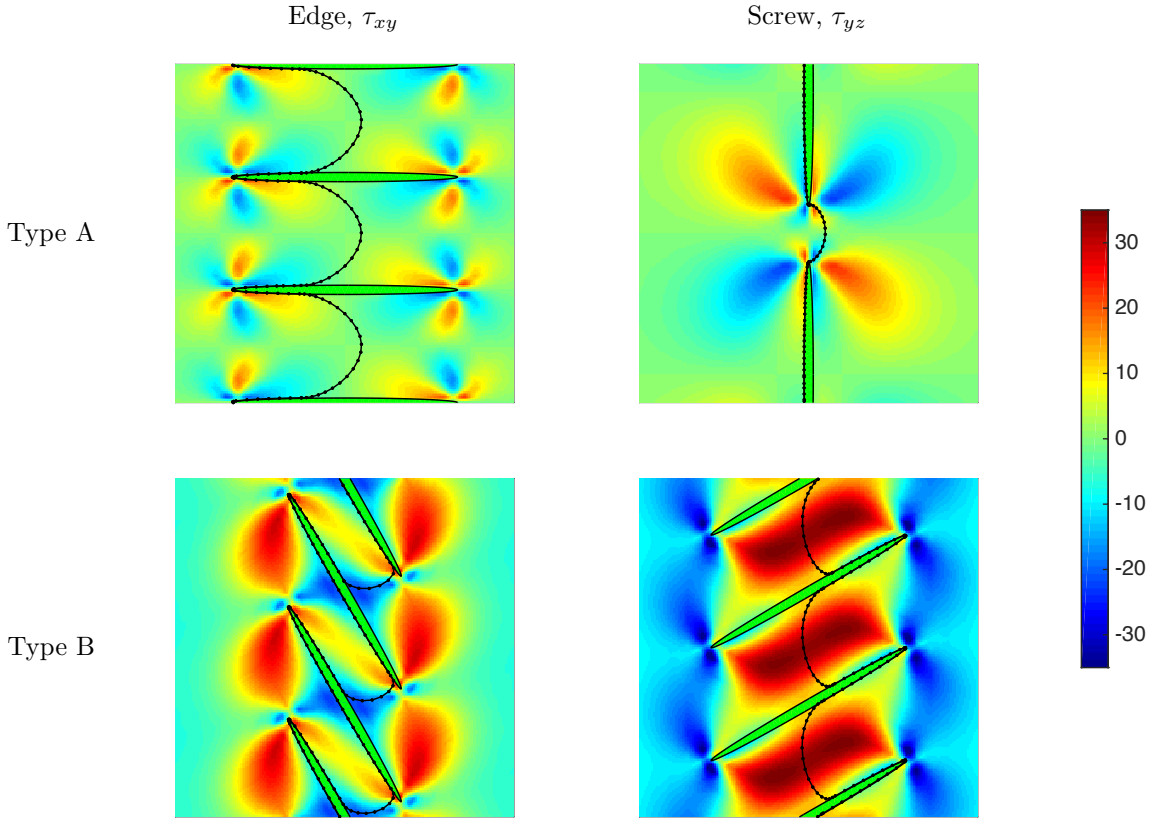


Figure 5.6: Misfit shear stress fields,  $\tau_{xy}$  and  $\tau_{yz}$  (in units of MPa), for a periodic array of  $\theta'$  precipitates. Showing all four geometries used in Orowan looping simulations. Precipitate spacing is  $L/d = 0.5$  for all except Type A screw dislocation, which has  $L/d = 2.5$ . We also show the dislocation configuration just below the looping stress. See Fig. 5.5(b) for information about the coordinate system and Burgers vector.

complex, with the stress field changing signs multiple times, making it unclear how the Orowan looping process will be influenced by the misfit field. Also note that the Type B misfit fields exhibit higher stresses.

#### *Orowan looping*

Fig. 5.7 presents the looping stress results for the configurations shown in Fig. 5.6 with respect to the separation distance between precipitate centers normalized by the major diameter,  $L/d$ . With misfit fields, we present results when the dislocation approaches from the left (blue diamonds) and

right (red squares) sides of the precipitate array. Results without a misfit field are shown as green dots. Also shown are curves for two different models which we will introduce in the discussion. For both a screw and edge dislocation, the Type A misfit field influences the looping stress negligibly. In contrast, the Type B misfit field has a modest impact on the looping stress when the precipitates are closely spaced. Both increases and reductions in the looping stress are observed, however the response is asymmetrical, with increases in the flow stress being more common. We will explore the implications of this asymmetry in the discussion.

To further examine the nature of the looping process, we show in Fig. 5.6 dislocation configurations just below the looping stress. These snapshots show that the precipitate collision detection and remeshing algorithms provide for an efficient and accurate representation of the Orowan looping process on the surface of the ellipsoid. With Type A precipitates, we see that the line is bowed out symmetrically, as is observed during classical Orowan looping around spherical precipitates [10]. In the Type B cases, the geometry is very different, with the dislocation line tilted as it extrudes through the channel between the precipitates. Examining the position of the dislocation line within the channel in these cases makes the influence of the misfit field clear. The edge dislocation approaching from the left side is impeded by the small (blue) region of negative stress. Looping with the screw dislocation from the right side is hindered by the large (red) region of positive shear stress. Strengthening is observed relative to the misfit-free looping stress in both of these cases by about 12.5 and 22.5 MPa for the edge and screw, respectively. These increments in the looping stress are consistent with the magnitude of the misfit field in the regions containing the dislocation line in Fig. 5.6.

### Discussion

In order to make comparisons with the BKS expression and develop a new analytical model to explain our results, we need to account for the dislocation core energy and consider the looping

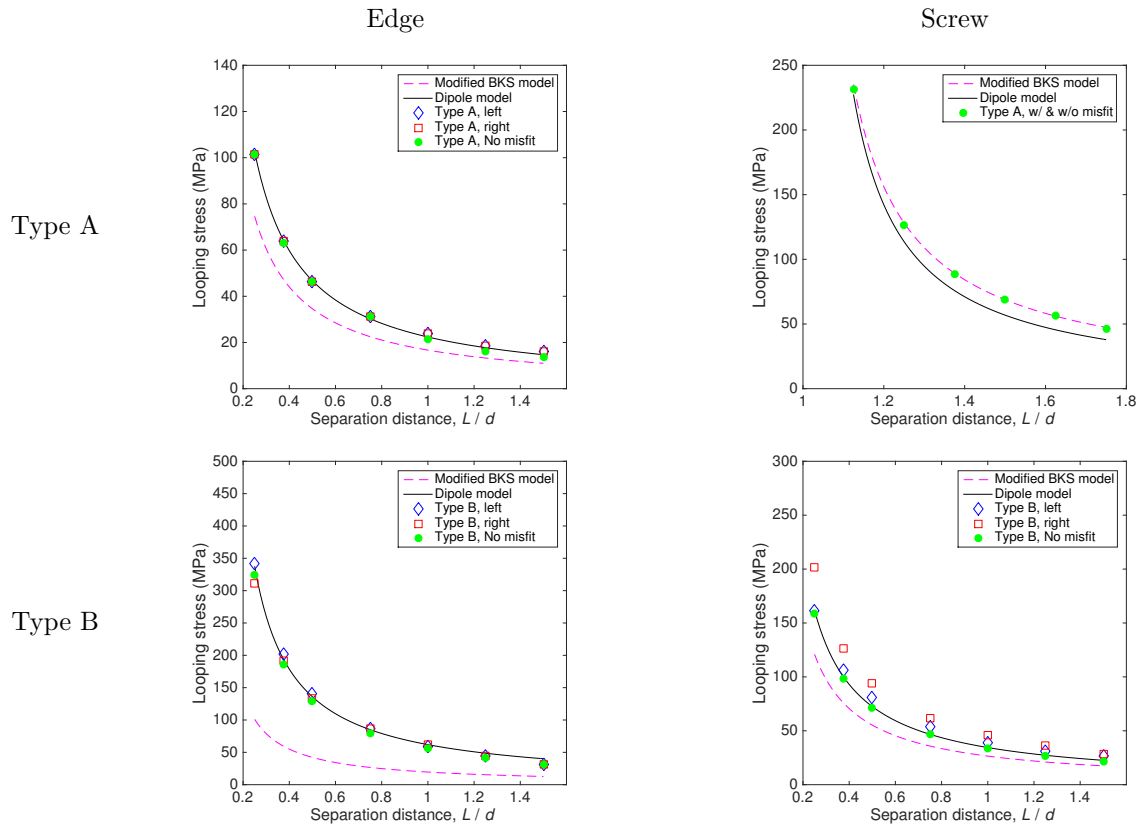


Figure 5.7: Looping stress results. Showing results with and without misfit stress fields approaching the precipitates shown in Fig. 5.6 from the left and the right sides.

geometry in more detail. We will show that there are two regimes for Orowan looping: a bow-out-limited regime where a modified version of the BKS expression holds and a dipole-limited regime where a new dipole-based model is needed.

#### *Core energy*

The analysis employed by Bacon et al. [10] did not include core energy effects, whereas we have included core energy in our simulations. **ParaDiS** uses a character-angle-dependent core energy function of the form

$$E_{\text{core}}(\phi) = E_c b^2 \left( \frac{\sin^2 \phi}{1 - \nu} + \cos^2 \phi \right), \quad (5.44)$$

where  $E_c$  is a parameter specified in Table 5.1 on the basis of atomistic calculations [177]. The core energy contributes to the line tension, adding a contribution to the looping stress of  $2E_{\text{core}}(90^\circ)/[b(L-d)]$  for an initially screw dislocation and  $2E_{\text{core}}(0^\circ)/[b(L-d)]$  for an initially edge dislocation. We will also make use of the core energy expression when computing the energy of a dislocation dipole below.

#### *Elliptical geometry*

Next we need to consider the looping geometry more carefully before we can develop analytical models to explain our results. Because the glide plane intersects the precipitate at a skewed angle, the dimensions and orientation of the ellipse encountered by the gliding dislocation are unknown without additional analysis. The geometry in the glide plane is shown in Fig. 5.8(a). Let  $\hat{r}_1$  and  $\hat{r}_2$  be the radii of the ellipse and  $\omega$  be the angle between the dislocation line and the major axis of the ellipse. To compute the dimensions of the ellipse formed by the ellipsoid-glide plane intersection, we use the method of Klein [83]. For a plane with unit normal  $\mathbf{n} = [n_1 \ n_2 \ n_3]^T$  in the coordinate system of the ellipsoid located a distance  $\kappa$  from the ellipsoid's center, his approach gives the radii

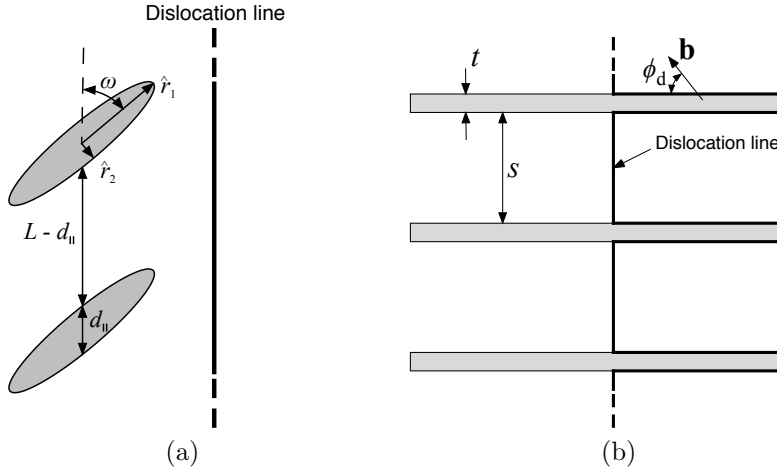


Figure 5.8: Geometry for looping models. (a) Geometry in the glide plane, with ellipses of radii  $\hat{r}_1$  and  $\hat{r}_2$  and diameter  $d_{\parallel}$  parallel to the dislocation line. (b) Schematic depiction of the Orowan looping process around plate-like precipitates of thickness  $t$  separated by channels of width  $s$ .

of the ellipse as

$$\hat{r}_i = \sqrt{\frac{1-\delta}{\beta_i}} \quad (5.45)$$

where  $i = 1, 2$ ,

$$\delta = \frac{\kappa^2}{r_1^2 n_1^2 + r_2^2 n_2^2 + r_3^2 n_3^2}, \quad (5.46)$$

and  $\beta_i$  are the roots of the quadratic expression

$$\beta^2 - \left[ n_1^2 \left( \frac{1}{r_2^2} + \frac{1}{r_3^2} \right) + n_2^2 \left( \frac{1}{r_1^2} + \frac{1}{r_3^2} \right) + n_3^2 \left( \frac{1}{r_1^2} + \frac{1}{r_2^2} \right) \right] \beta + \left( \frac{n_1^2}{r_2^2 r_3^2} + \frac{n_2^2}{r_1^2 r_3^2} + \frac{n_3^2}{r_1^2 r_2^2} \right) = 0. \quad (5.47)$$

We take  $\hat{r}_1 > \hat{r}_2$  ( $\beta_1 < \beta_2$ ) as a convention.

Applying these methods to the  $\theta'$  geometry with the glide plane passing through the center of the precipitate, we obtain elliptical dimensions of  $\hat{r}_1 = 2000 \text{ \AA}$  and  $\hat{r}_2 \approx 81.6 \text{ \AA}$ . Note that if the precipitate was disk-shaped rather than ellipsoidal, this same analysis would also work for determining the in-plane geometry (the thickness and length of the disk's rectangular cross-section).

*Bow-out-limited looping*

In the bow-out-limited looping regime, the looping stress is governed by line tension arguments in the same way it is in the BKS model. Since the shape of the precipitate in the glide plane is not circular, the BKS relationship cannot be used directly. We can modify the BKS expression in any number of ways. For reasons to be made clear below, we will choose the following modification. In place of the spherical precipitate's diameter, we will use the largest width of the ellipse in the direction parallel to the initial dislocation line, denoted as  $d_{\parallel}$ . As shown in Fig. 5.8(a), this corresponds to the diameter of the ellipse at an angular position  $\omega$  from the major axis of the ellipse, given by

$$d_{\parallel} = \frac{2\hat{r}_1\hat{r}_2}{\sqrt{\hat{r}_1^2 \sin^2 \omega + \hat{r}_2^2 \cos^2 \omega}}. \quad (5.48)$$

Use of this diameter means that the length of the dislocation line bowing out is assumed to be  $L - d_{\parallel}$ . However, examination of bow out configurations from simulations shows that this is often not the case. Nonetheless, we select this diameter for use in the BKS expression for its simplicity, and because  $d_{\parallel}(\omega = 0^\circ) = 2\hat{r}_1$  and  $d_{\parallel}(\omega = 90^\circ) = 2\hat{r}_2$ , i.e., it recovers the major and minor elliptical diameters when the dislocation is parallel and orthogonal to the ellipse's major axis.

Using  $d_{\parallel}$  in the BKS expression and incorporating core energy effects leads to the following looping stress expression:

$$\tau_{\text{BKS}}^{\parallel} = A \frac{\mu b}{(L - d_{\parallel})} \left[ \ln \left( \frac{X_{\parallel}}{r_c} \right) + B \right] + \frac{2E_{\text{core}}}{b(L - d_{\parallel})} \quad (5.49)$$

where

$$X_{\parallel} \equiv \left[ (L - d_{\parallel})^{-1} + d_{\parallel}^{-1} \right]^{-1}. \quad (5.50)$$

In Fig. 5.7 we show the looping stress predictions using the modified BKS expression, Eq. (5.49), as dashed lines. If the modified expression captures the physics of the looping process, it should match well the data with no misfit stresses. We have selected the fitting constant  $B$  to optimize

the fit with the data for a screw dislocation interacting with a Type A precipitate (i.e.,  $\omega = 0^\circ$ ), finding  $B = -1.3$ . Note that with this choice the modified expression fits the data very well. In all other cases, however, the modified BKS expression underpredicts the looping stress, being about 70% below the simulation results in the case of an edge dislocation and a Type B precipitate. We have tested other modifications of the BKS expression as well and none capture all of the trends in the simulation results. The failure of the modified BKS model motivates us to develop a new model for Orowan looping.

#### *Dipole-limited looping*

Fig. 5.7 shows that a bow-out-based picture of Orowan looping does not fully characterize the process of loop formation with the high aspect ratio ellipsoids we have used in our simulations. Instead, we consider the looping process in terms of the formation of a dislocation dipole. It was proposed by Russell and Ashby [142] that the energy of an Orowan loop around a  $\theta'$  precipitate can be approximated as the energy of a dipole whose separation distance is equal to thickness of the precipitate in the glide plane. Here we make use of this approximation to develop a new model for Orowan looping.

Consider the schematic depiction of Orowan loop formation given in Fig. 5.8(b), where loops form around an array of platelets of thickness  $t$  with channels of width  $s$  separating them. In order to derive the shear stress necessary to form an Orowan loop, we apply the principle of virtual work. As the dislocation segments in the channels between precipitates glide forward, they extend in length the dipoles surrounding the precipitates. The critical condition for this process to occur spontaneously without an increase in stress is that the work done by the external stress,  $W$ , balances the energy necessary to grow the dipole,  $\mathcal{E}$ . The work done by the external stress upon moving the gliding dislocation segment a distance  $\Delta x$  is  $W = \tau b \Delta x$ . The energy of a dipole of length  $\Delta x$  is

approximately

$$\mathcal{E} = \Delta x [E_d^{\text{el}} + E_d^{\text{core}}]. \quad (5.51)$$

The core energy per unit length of the dipole is simply

$$E_d^{\text{core}} = 2E_{\text{core}}(\phi_d) \quad (5.52)$$

where  $\phi_d$  is the character angle of the dipole ( $\phi_d = 0^\circ$  for Type A and  $\phi_d = 60^\circ$  for Type B). In the nonsingular theory of dislocations used in ParaDiS, the elastic energy per unit length of a dipole is [20]

$$E_d^{\text{el}}(\phi_d) = \frac{\mu b^2}{2\pi} \left( \frac{\sin^2 \phi_d}{1 - \nu} + \cos^2 \phi_d \right) \ln \left( \frac{t}{r_c} \right) + \frac{\mu b^2}{4\pi} \cos^2 \phi_d. \quad (5.53)$$

Equating the work done and the increase in energy of the dipole, we arrive at a looping stress of

$$\tau_d = \frac{\mu b}{2\pi s} \left[ \left( \frac{\sin^2 \phi_d}{1 - \nu} + \cos^2 \phi_d \right) \ln \left( \frac{t}{r_c} \right) + \frac{1}{2} \cos^2 \phi_d \right] + \frac{2E_{\text{core}}(\phi_d)}{sb}. \quad (5.54)$$

To apply this expression to the elliptical geometry used here, we approximate the dipole separation distance  $t$  as the minor diameter in the glide plane,  $2\hat{r}_2$ , and by simple geometry find that  $s = t - L \sin \omega$ . The results for each of the cases are shown as solid black lines in Fig. 5.7. We see that in three of the four cases, the model fits the simulation results without a misfit field incredibly well. This fit is achieved without any tuned fitting constants. Even in the case where bow-out governs looping (screw with Type A), the dipole model fits reasonably well, with errors of less than 20%.

#### *Misfit fields*

A significant finding in this work is the asymmetry observed between strengthening and weakening induced by a misfit field. As shown in Fig. 5.7, with the type B precipitates, the same misfit field strengthens more readily and more significantly than it weakens. In contrast, a naive analysis

would expect that the same misfit field would weaken and strengthen symmetrically. The observed asymmetry appears to be a result of the plate-like geometry of these precipitates. The dipole-limited model is based on the concept of a steady-state configuration, meaning that the looping stress is independent of the length of the dipole. As a result, the looping stress must be applied during the entire time the dislocation extrudes between the platelets in order for Orowan looping to occur. Hence, the region in the channel with the highest repulsive misfit force entirely governs the influence of the misfit field. This fact makes misfit weakening very difficult, because the misfit field must be attractive through the entire channel to result in the overall looping stress being reduced. If only a small region of the channel is weakened, the looping stress will still be unchanged in the rest of the channel, making the overall looping stress unchanged. In contrast strengthening is readily accomplished with this geometry; increasing the looping stress over a small region of the channel has the same effect as increasing it over the whole channel. We see this in the Type B-edge case shown in Fig. 5.6, where the dislocation is pinned by the small region of negative stress.

To test these ideas out more explicitly, a simple set of simulations was performed. A special misfit field was imposed on the Type B geometry with an edge dislocation using a precipitate spacing of  $L/d = 0.5$ . In the absence of a misfit field, the looping stress was computed to be  $46.25 \pm 2.5$  MPa for this geometry. The special misfit field was such that a shear stress of 50 MPa was imposed over a region of width  $0.1d$  down the center of the precipitate array, and zero everywhere else. With this field, the dislocation line only experiences a misfit force when extruding through the central region of the array. The looping stress was then computed when approached from both sides of the array; the resulting looping stresses were  $46.25 \pm 2.5$  and  $86.25 \pm 2.5$  MPa, resulting in changes of 0 and 40 MPa relative to the misfit-free solution. Hence, strengthening is much more readily attained than weakening, exactly as predicted above.

Note that these arguments do not hold in the bow-out-limited regime, where Orowan looping occurs when a critical bow-out configuration is achieved. In this regime, the misfit field will operate more or less symmetrically in terms of strengthening and weakening, since a steady state configuration is not attained during looping. Based on this fact, we would expect that combining misfit strengthening with plate-like precipitates is relatively more robust and effective than when combined with other precipitate shapes that are governed by bow out (such as spheres).

### 5.3.2 Bulk plasticity

#### Precipitate microstructure generation

In order to study the plasticity of real aluminum-copper alloys, we need to be able to generate physically realistic precipitate microstructures. We can break down a precipitate microstructure for our studies into 5 key features: 1) the average precipitate diameter  $\bar{d}$ , 2) the average precipitate aspect ratio  $\bar{A}$ , 3) the probability distribution of precipitate diameters, 4) the number density of precipitates, and 5) the spatial distribution of precipitates. To characterize each of these features, we utilize the experimental transmission electron microscope measurements of Boyd and Nicholson [15] and Merle and Fouquet [108], and the atom-probe tomography measurements of Biswas et al. [14]. These researchers examined the microstructures of aluminum-copper alloys over a wide range of aging conditions, measuring precipitate dimensions and making qualitative observations of their distributions in space. We will in particular focus on Al-4 wt.% Cu that is aged for 3 to 10 hours at 200 to 300°C, because these conditions result in microstructures dominated by  $\theta'$  precipitates [14,15], and because single crystal experiments have been performed on these alloys [5,109,142,148].

First, we consider the average precipitate geometry (features 1 and 2 above). Boyd and Nicholson found that after 10 hours of aging, the average  $\theta'$  diameter  $\bar{d}$  was about 2000 Å and 6000 Å for aging at 200 and 240°C, respectively. Merle and Fouquet obtained similar results, with a mean diameter

of about 7000 Å after 10 hours at 240°C. Finally, Biswas et al. measured a mean diameter 1800 Å after 8 hours at 190°C (although they measured fewer precipitates than [15] and [108]). Given these results, we chose an average diameter of 4000 Å. In terms of the aspect ratios for the same respective conditions, Boyd and Nicholson found a uniform value of 45 for both of their aging conditions, Merle and Fouquet measured a much larger value of about 80, and Biswas et al. measured about 23. For our studies, we will use a value of 30 for all precipitates.

Consideration of the probability distribution for the diameters is more complex. The prevailing approach used in DD studies with precipitates [115] utilizes the Wagner-Lifshitz-Slyozov (WLS) distribution [102,174], which is derived under the assumption that precipitate coarsening is diffusion-limited—the case of so-called Ostwald ripening. However, both Boyd and Nicholson and Merle and Fouquet found that the distributions for  $\theta'$  precipitates deviated significantly from the WLS expression, which they attributed to mean that  $\theta'$  coarsening and nucleation is not diffusion-controlled. Therefore, we use their experimentally measured distributions directly for our simulations. Fig. 5.9 presents the probability density data for the precipitate diameter normalized by the average diameter,  $d/\bar{d}$ , obtained by Boyd and Nicholson after 4 hours at 200°C and by Merle and Fouquet after 10 hours at 225°C. By trial and error, we find that these data are very well characterized by gamma distributions. Since the average normalized diameter is  $d/\bar{d} = 1$ , the two parameter gamma distribution reduces to a single parameter distribution of the form

$$p\left(\frac{d}{\bar{d}}\right) = \frac{1}{k^{-k}\Gamma(k)} \left(\frac{d}{\bar{d}}\right)^{k-1} \exp\left(-k\frac{d}{\bar{d}}\right) \quad (5.55)$$

where  $p(d/\bar{d})$  is the probability density for diameter  $d$ ,  $\Gamma(\cdot)$  is the gamma function, and  $k$  is the parameter controlling the shape of the distribution. The distributions obtained by Boyd and Nicholson and Merle and Fouquet are fit well by gamma distributions with  $k = 4.75$  and  $4.31$ , respectively. Fig. 5.9 shows the gamma distribution with  $k = 4.75$ ; in our simulations, we randomly sample this

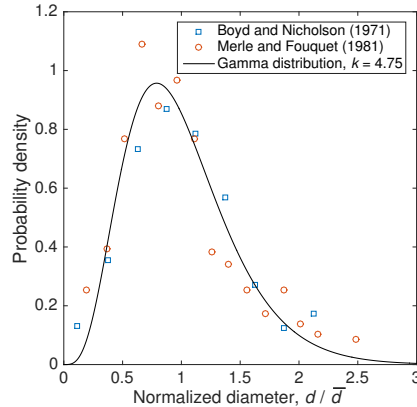


Figure 5.9: Probability density data for  $\theta'$  precipitates. Experimental data from Boyd and Nicholson [15] after aging for 4 hours at 200°C and Merle and Fouquet [108] after aging for 10 hours at 225°C are shown, along with the single parameter gamma distribution of Eq. (5.55) with  $k = 4.75$ .

distribution to determine precipitate diameters.

In terms of the number density of precipitates (number of precipitates per unit volume), Biswas et al. measured densities of  $1.51 \times 10^{21} \text{ m}^{-3}$  and  $1.47 \times 10^{20} \text{ m}^{-3}$  with alloys aged for 8 hours at 190°C and 4 hours at 260°C, respectively. We will use a value of  $1 \times 10^{20} \text{ m}^{-3}$  in our simulations.

Finally, we must arrange the precipitates in space. There have been three major approaches used for placing obstacles in DD simulations. In the first, obstacles are simply placed randomly (or close to randomly) [139]. In the second, obstacles are placed according to a distribution characterizing their separation, such as a radial distribution function [182]. And in the third approach, obstacles are placed so that the separation distance between two obstacles scales with their diameters [112, 117]. Again, similar to the WLS distribution, the assumption underlying this approach is that precipitate growth is diffusion-limited, so that each precipitate generates a solute-poor denuded zone around it proportional in size to the precipitate diameter, thus preventing other precipitates from forming in this region. To our knowledge, there have been no quantitative studies of  $\theta'$  spatial distributions. A number of qualitative observations have been made, however. Boyd and Nicholson observed that at earlier aging times, such as those considered here, precipitates occupying the same habit

plane had a tendency to cluster near each other, even coalescing at times, with relatively large separation distances between clusters. In contrast, they observed that precipitates on different habit planes never intersected each other. These trends are partly explained by the observation that  $\theta'$  precipitates nucleate on dislocations [15], which can lead to clustering. Additionally, Vaithyanathan et al. [170] have observed in phase field simulations of coarsening the tendency for coalescence of same-planed precipitates and repulsion of unlike-planed precipitates, arguing that minimization of interfacial energy is the driving force.

Given all of these observations, we employ the following simple procedure for precipitate placement. For each precipitate, an  $\{001\}$  habit plane is selected at random and a precipitate diameter is selected at random from the gamma distribution. The precipitate is then placed randomly within the simulation cell subject to a single condition: it cannot intersect a precipitate lying on a different habit plane. The constraint that new precipitates cannot intersect with existing precipitates on differing habit planes automatically leads to clustering of platelets on parallel planes. This leads to clumps of precipitates with common habit planes, as is observed experimentally. Fig. 5.10(a) presents a TEM image from Biswas et al. [14] of a  $\theta'$  microstructure after 8 hours at 190°C and (b) shows a “thin foil” with a 0.1  $\mu\text{m}$  thickness taken from a precipitate microstructure generated using the above parameters and procedures. Note that in the TEM image only precipitates in habit planes orthogonal to the page are visible, and so we present our microstructure in the same way. Fig. 5.10(c) shows an isometric view of all precipitates in the microstructure. The simulation cell in this figure is a 2  $\mu\text{m}$  cube.

## Results

A dislocation structure was initialized as 25 straight lines with a 60° character angle positioned randomly, and assigned random  $\langle 110 \rangle$  Burgers and  $\{111\}$  glide planes. Because of the random positioning, some dislocation lines were initially piercing precipitates; segments initially piercing

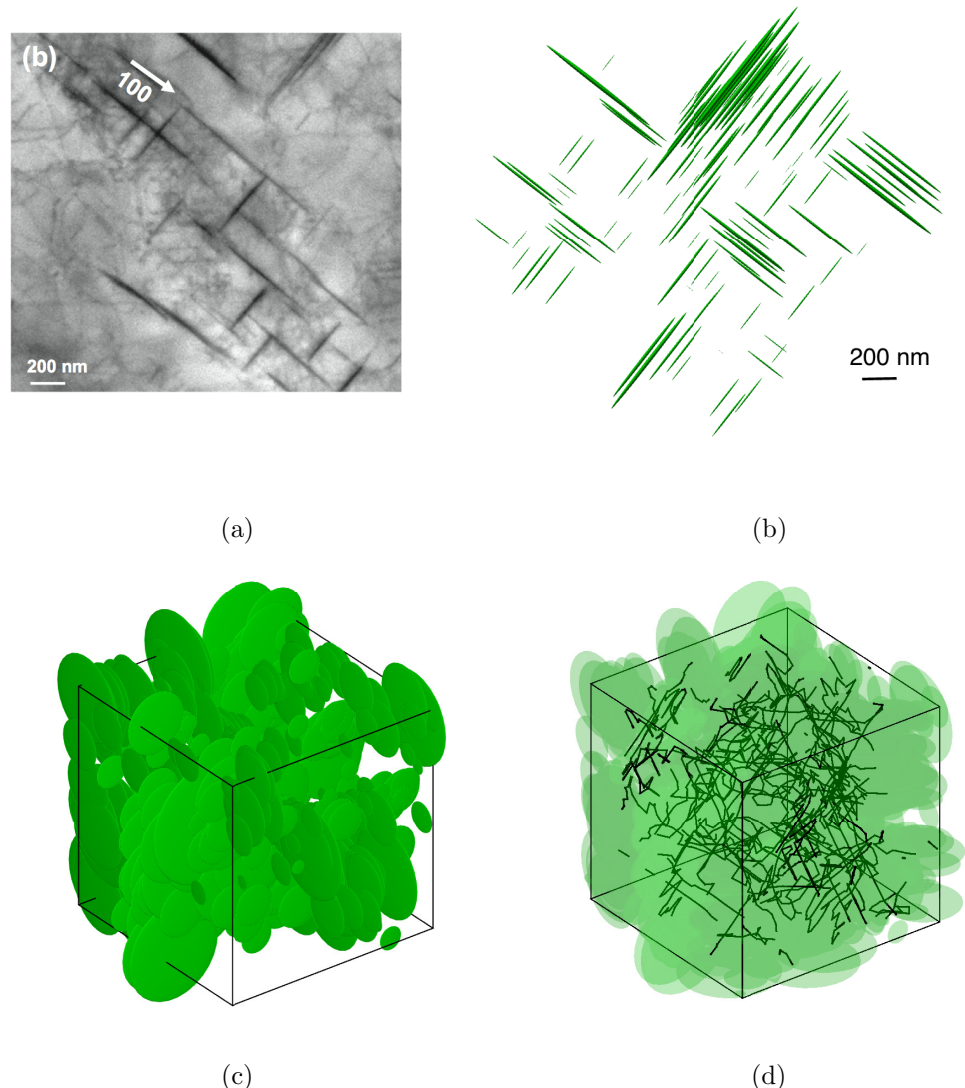


Figure 5.10: Microstructures of  $\theta'$  precipitates. (a) TEM micrograph of Al-4 wt.% Cu aged for 8 hours at 190°C from Biswas et al. [14]. (b) “Thin foil” with a  $0.1 \mu\text{m}$  thickness taken from a microstructure generated using procedure and parameters provided in the text. Precipitates parallel to the page are not shown. (c) Isometric view of the precipitate microstructure in (b) with all precipitates shown. (d) Dislocation structure after 0.02% plastic strain using an initial structure with 25 straight dislocation lines. The simulation cell is a  $2 \mu\text{m}$  cube.

precipitates were allowed to move freely through the precipitate until they exited it. The simulation cell was then loaded by a fixed axial stress of 500 MPa in the [0 0 1] direction; unfortunately, the presence of the precipitates causes the time step to be very small ( $\sim 10^{-13}$  s), making it difficult to simulate a stress-strain curve under strain-control at present. Future work will focus on coupling the new integrator developed in Chapter 2 with the precipitates code to improve the efficiency and overcome this issue.

Fig. 5.10(d) presents a snapshot of the simulation after a plastic strain of 0.02%. We see that a highly tangled structure has developed, with a large number of Orowan loops.

## 5.4 Conclusions

We have developed and implemented a new DD precipitates algorithm that allows for arbitrarily-shaped ellipsoids with arbitrary misfit. The four pillars of this algorithm—collision detection, remeshing, obstacle cutting, and misfit force calculation—integrate straightforwardly into the DD architecture. We believe that our approach to collision detection is particularly novel and robust. The new capabilities provided by this algorithm enable studies of plasticity in precipitation strengthened alloys with non-spherical and non-cuboidal precipitates, alloys which were previously very difficult or impossible to study.

With our simulations of Orowan looping, we have shown that the traditional view of Orowan looping is inaccurate when precipitates are plate-like. Instead, a model based on the formation of a dipole across the precipitate very accurately captures the physics of loop formation. Even in the case of a screw dislocation bypassing a Type A precipitate, for which the traditional bow-out-limited model holds, the new dipole-limited model is accurate to within 20%. The new model for Orowan looping can be applied to better understand plasticity in materials containing plate-like precipitates. It could even be applied to other materials where Orowan looping occurs in a similar manner to that

studied here. For instance, materials with impenetrable cuboidal precipitates may also be governed by dipole formation, since they have narrow channels through which dislocations must extrude.

Our examination of the role of the misfit field has illuminated a number of aspects of misfit strengthening. First, we have shown that the misfit fields of precipitates with non-dilatational misfits can be complex, so that their effects cannot be determined straightforwardly by simple inspection. For example, the misfit field for an edge dislocation with a Type B precipitate changes sign multiple times around the precipitates. This result shows the merit of DD simulations for studying these systems. Secondly, we have identified that plate-like precipitates with misfit fields have an intrinsic strengthening-weakening asymmetry; strengthening is much more readily achieved than weakening. This derives from the nature of the Orowan looping process, which occurs by steady state elongation of a dipole rather than by reaching a critical bow out geometry. This result indicates that coupling dispersion and misfit strengthening with plate-like precipitates is an efficient mode for precipitation strengthening.

Our ultimate goal is to employ the new precipitates capability to study large-scale plasticity in precipitation hardened alloys, much like the study on pure metals in Chapter 3. We have developed a basic algorithm for generating precipitate microstructures, and shown that they compare reasonably well with real materials. Further analysis of experimental microstructures—for example, better quantifying how precipitates are distributed in overaged aluminum-copper—would enable even more accurate simulations. Presently large-scale tensile test simulations are slow and difficult to utilize due to time step limitations. We hope to accelerate these simulations in the near future and enable large-scale studies of precipitation strengthened alloys.